

## Understanding contact angle hysteresis on an ambient solid surface

Yong Jian Wang,<sup>1</sup> Shuo Guo,<sup>1</sup> Hsuan-Yi Chen,<sup>2,3,4</sup> and Penger Tong<sup>1,\*</sup>

<sup>1</sup>*Department of Physics, Hong Kong University of Science and Technology, Clear Water Bay, Kowloon, Hong Kong*

<sup>2</sup>*Department of Physics, National Central University, Zhongli 32001, Taiwan, Republic of China*

<sup>3</sup>*Institute of Physics, Academia Sinica, Taipei 11520, Taiwan, Republic of China*

<sup>4</sup>*Physics Division, National Center for Theoretical Sciences, Hsinchu 30113, Taiwan, Republic of China*

(Received 7 May 2014; revised manuscript received 18 November 2015; published 12 May 2016)

We report a systematic study of contact angle hysteresis (CAH) with direct measurement of the capillary force acting on a contact line formed on the surface of a long glass fiber intersecting a liquid-air interface. The glass fiber of diameter 1–2  $\mu\text{m}$  and length 100–200  $\mu\text{m}$  is glued onto the front end of a rectangular cantilever beam, which is used for atomic force microscopy. From the measured hysteresis loop of the capillary force for 28 different liquids with varying surface tensions and contact angles, we find a universal behavior of the unbalanced capillary force in the advancing and receding directions and the spring constant of a stretched meniscus by the glass fiber. Measurements of the capillary force and its fluctuations suggest that CAH on an ambient solid surface is caused primarily by two types of coexisting and spatially intertwined defects with opposite natures. The contact line is primarily pinned by the relatively nonwetting (repulsive) defects in the advancing direction and by the relatively wetting (attractive) defects in the receding direction. Based on the experimental observations, we propose a “composite model” of CAH and relevant scaling laws, which explain the basic features of the measured hysteresis force loops.

DOI: [10.1103/PhysRevE.93.052802](https://doi.org/10.1103/PhysRevE.93.052802)

### I. INTRODUCTION

Contact angle hysteresis (CAH), where the motion of a contact line (CL) between a liquid interface and a solid substrate is pinned by the physical roughness and/or chemical heterogeneity on the solid surface, is an outstanding problem in interfacial dynamics and has been with us for many years [1–4]. The contact line pinning causes the contact angle between the liquid and solid surfaces to depend on the direction of fluid motion [1]. While considerable progress has been made recently in controlling the wettability of various textured solid surfaces [5,6] and in understanding the energetics associated with deformable soft substrates [7–9], one still has a poor understanding of CAH. This is particularly true for many ambient solid surfaces of interest [3]. Up to now, we do not have quantitative theoretical or experimental answer to such simple questions as how CAH is determined by the basic features of the substrate-fluid interactions [3,4].

In 1984, Joanny and de Gennes [10] proposed a model (JG model) to explain CAH by considering the pinning effect of individual defects. In particular, they calculated CAH for a single defect based on a mechanical balance between the elastic restoring force due to the deformation of the liquid interface and the pinning force. Since then many experiments have been carried out focusing mainly on simple model systems with a single or a regular array of synthetic defects with sizes varied from milli- or micrometers [11–16] to nanometers [17–19]. While these experiments provided useful information about CAH at the single defect level, our understanding of CAH for ambient surfaces, which have real-world features such as irregular overlapping defects at different length scales, is still limited. The lack of experimental progress is partially due to the fact that direct observation of the contact angle in the

immediate vicinity ( $\lesssim 1 \mu\text{m}$ ) of a moving contact line (MCL) is difficult with conventional optical methods [20,21]. As a result, most contact angle measurements were conducted in the region 10–20  $\mu\text{m}$  away from the core region of MCL. The pinning of a CL at the microscopic level causes the CL dynamics to be very sensitive to the distance away from it, at which measurements are made [2–4]. These features make CAH a truly multiscale phenomenon. Direct measurements of CAH at the CL and capillary force fluctuations are therefore needed in order to test different theoretical ideas.

Recently, we developed a hanging fiber probe based on atomic force microscopy (AFM) for the study of interfacial dynamics [22,23]. As shown in Fig. 1, the “long needle” AFM involves a vertical glass fiber of diameter  $d \simeq 1.6 \mu\text{m}$  and length 95  $\mu\text{m}$ , which is glued onto the front end of a rectangular AFM cantilever. As a sensitive mechanical resonator, the hanging fiber probe can accurately measure a minute change of its viscous damping, when the fiber tip touches a liquid-air interface, at which a circular CL between the liquid interface and fiber surface is formed. In recent experiments [24,25], this “long needle” AFM was fully calibrated and used to measure the friction coefficient of a fluctuating CL. The hanging fiber probe shown in Fig. 1 can also serve as an accurate force apparatus capable of measuring the capillary force [26,27],

$$f(t) = -\pi d \gamma \cos \theta_i(t), \quad (1)$$

acting on the circular CL. In the above,  $\pi d$  is the CL length and  $\theta_i$  is the contact angle. The sign of  $f$  is defined as  $f \leq 0$  for  $\theta_i \leq 90^\circ$  and  $f > 0$  for  $\theta_i > 90^\circ$ .

In this paper, we report a systematic experimental study of CAH using the AFM-based capillary force apparatus. By accurately measuring the hysteresis loop of the capillary force for 28 different liquids with varying surface tensions and contact angles with the glass fiber, we find a universal behavior of the elastic restoring force of the pinned liquid interface and the unbalanced capillary force in the advancing

\*Corresponding author: [penger@ust.hk](mailto:penger@ust.hk)

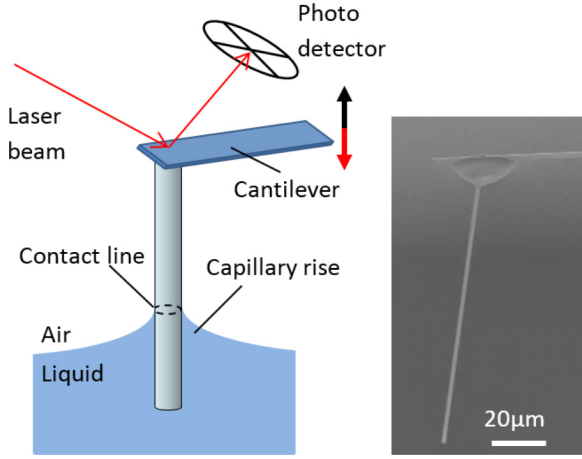


FIG. 1. Sketch of the AFM-based capillary force apparatus and scanning electron microscope image of the actual hanging glass fiber of diameter  $d \simeq 1.6 \mu\text{m}$  and length  $95 \mu\text{m}$ .

and receding directions. The experiment demonstrates that CAH is caused primarily by two different sets of relatively wetting and nonwetting defects on the fiber surface.

The remainder of the paper is organized as follows. We first describe the working principle of the AFM-based capillary force apparatus in Sec. II. The experimental procedures and sample preparation methods are also presented in Sec. II. The experimental results and further discussions are given, respectively, in Secs. III and IV. Finally, the work is summarized in Sec. V.

## II. EXPERIMENT

### A. Working principle of the AFM-based capillary force apparatus

Figure 1 shows the working principle and the actual setup of the AFM-based capillary force apparatus. By moving the fiber up or down through the liquid interface at a constant speed  $U$ , one can use AFM to accurately measure the capillary force acting on the MCL as a function of time  $t$  or traveling distance  $s = Ut$  [see Eq. (1)]. When there is no hysteresis in the advancing and receding directions, the measured steady-state force is very smooth with little fluctuations and  $\theta_i(t)$  takes the equilibrium value  $\theta_0$ . For instance, with a freshly plasma cleaned glass fiber, we find the value of  $\theta_0$  for the water-air interface is zero and little hysteresis is observed (see Table I). For many other liquids listed in Table I, however, the advancing force  $f_a (= \pi d \gamma \cos \theta_a)$  measured when the fiber is pushed downward is smaller than the receding force  $f_r (= \pi d \gamma \cos \theta_r)$  when the fiber is pulled upward. Therefore, the resulting advancing contact angle  $\theta_a [= \cos^{-1}(f_a / \pi d \gamma)]$  is larger than the receding contact angle  $\theta_r [= \cos^{-1}(f_r / \pi d \gamma)]$ . It is also found that fluctuations of the steady-state force increase with CAH, which is characterized by the capillary force difference per unit length

$$f_h \equiv \gamma(\cos \theta_r - \cos \theta_a), \quad (2)$$

where the mean values of  $f_a$  and  $f_r$  are used to define  $\theta_a$ ,  $\theta_r$ , and  $f_h$ .

TABLE I. Twenty-eight liquid samples used in the experiment and their literature values of viscosity  $\eta$ , density  $\rho$ , and surface tension  $\gamma$  at  $25^\circ\text{C}$  [28]. The values of the advancing contact angle  $\theta_a$  and receding contact angle  $\theta_r$  are obtained in the present experiment (see text for more details).

Liquids	$\eta$ (cP)	$\rho$ (g/cm <sup>3</sup> )	$\gamma$ (mN/m)	$\theta_a$ ( $^\circ$ )	$\theta_r$ ( $^\circ$ )
Methanol	0.54	0.792	22.07	0	0
Ethanol	1.07	0.789	21.97	0	0
1-Propanol	1.95	0.803	23.32	0	0
Isopropanol	2.04	0.786	20.93	0	0
Butanol	2.54	0.81	24.93	$15.9 \pm 1.0$	$9.0 \pm 1.8$
Penanol	3.62	0.814	25.44	$21.0 \pm 0.8$	$15.5 \pm 1.0$
Hexanol	4.58	0.814	25.81	$28.5 \pm 0.8$	$23.8 \pm 1.0$
Octanol	7.29	0.824	27.1	$33.6 \pm 0.5$	$28.4 \pm 0.6$
Anylamine	0.70	0.755	24.69	$12.9 \pm 2.0$	$5.8 \pm 4.5$
Hexylamine	0.60 <sup>a</sup>	0.766	25.75	$19.3 \pm 1.5$	$13.4 \pm 2.1$
Heptylamine	1.31	0.774	20.52	$27.8 \pm 1.1$	$23.6 \pm 1.3$
Octanamine		0.782	26.12	$29.8 \pm 1.6$	$23.8 \pm 2.0$
Acephenone	1.69	1.028	39.04	$29.7 \pm 0.8$	$20.9 \pm 1.3$
Anisole	1.06	0.995	35.1	$24.9 \pm 1.3$	$19.2 \pm 1.6$
Benzyl alcohol	5.47	1.044	40.58	$33.0 \pm 1.4$	$24.9 \pm 1.8$
Methyl benzoate	1.67	1.084	38.75	$25.6 \pm 1.2$	$20.7 \pm 1.5$
<i>o</i> -Xylene	0.76	0.87	32.59	$8.4 \pm 2.0$	$6.0 \pm 2.7$
Formic acid	1.61	1.22	37.13	$35.2 \pm 1.0$	$22.2 \pm 1.7$
Acetic acid	1.06	1.049	27.1	$9.1 \pm 2.8$	$3.0 \pm 8.3$
Propanoic acid	1.03	0.99	26.2	0	0
Butyric acid	1.43	0.960	26.05	0	0
Valeric acid	2.2	0.930	26.1	$9.9 \pm 2.5$	$8.6 \pm 2.8$
Hexanoic acid		0.93	27.55	$15.4 \pm 2.9$	$5.4 \pm 8.3$
Heptanoic acid	3.84	0.918	27.76	$22.6 \pm 1.9$	$18.2 \pm 2.3$
Octanoic acid	5.02	0.910	28.7	$22.2 \pm 2.2$	$15.0 \pm 3.3$
Decane	0.84	0.736	23.37	0	0
FC 77	1.3	1.78	13	0	0
Water (H <sub>2</sub> O)	0.89	1.00	72	0	0

<sup>a</sup>This value of  $\eta$  was obtained at  $35^\circ\text{C}$  [29].

The apparatus shown in Fig. 1 has several useful features for the study attempted here. (i) With an accurate calibration, the AFM can measure the capillary force down to 10 pN at the accuracy of 0.2%. (ii) Because  $\theta_i$  is determined directly by the capillary force acting on the MCL, it is the contact angle most relevant to CAH. (iii) By moving the fiber up or down through the liquid interface, one can immediately tell whether it is pinned or not and measure  $\theta_i$  at a high sampling rate (up to 1 MHz). Such a real-time measurement of  $\theta_i$  allows one to directly study the pinning-depinning dynamics of the MCL. (iv) Similar devices using a hanging fiber probe with diameter  $d \sim 25 \mu\text{m}$  [26] and  $d \sim 20 \text{nm}$  [19] have been used to study the wetting dynamics. In the present experiment, we use the glass fibers with diameter 1–2  $\mu\text{m}$  and length 100–200  $\mu\text{m}$ . The use of a micron-sized fiber provides a proper spatial averaging over the CL length  $\pi d$  for the study of stick-slip-like motion of the MCL over a wide dynamic range. This mesoscale CL length is long enough to avoid seeing peculiar effects of a few individual defects but is short enough so one can still observe large fluctuations in the measured capillary force. In addition, the overall dimension of the hanging fiber is designed so one can ignore the buoyancy force acting on the fiber

and have an easy operation in microassembly, fiber surface cleaning and treatment, and handling of liquid interfaces.

### B. Preparation of hanging fiber probe

The assembly of the hanging fiber probe is carried out under a high-magnification stereo-microscope using a motorized micromanipulator system. The thin glass fiber is pulled out of a capillary glass rod of diameter 1.0 mm using a pipette puller. A UV-curable glue (Norland, NOA 81) is used to permanently connect the glass fiber to the front end of a rectangular tipless cantilever beam. Commercial silicon microcantilevers (Nanosensors) with the spring constant  $k = 2 \text{ N/m}$  are used in the experiment. As shown in Fig. 1, the fiber was tilted at an angle  $11^\circ$  with respect to the cantilever normal so the hanging fiber becomes normal to the liquid-air interface when the cantilever is mounted to the AFM holder. In the experiment, the  $z$ -axis piezo of the AFM is used to move the fiber up or down at a constant speed  $U$ . As the fiber moves vertically, the circular CL sweeps over the surface of the glass fiber.

A freshly prepared glass fiber probe is cleaned using a low vacuum plasma cleaner at the power 40 W for 15 min before mounting it to the cantilever holder. The vacuum is kept at about 600 millitorr during the plasma cleaning. After the plasma cleaning, the glass fiber probe is examined under a scanning electron microscope (SEM) and no visible damage is found on the surface of the glass fiber and UV glue. The plasma cleaning is also conducted at the power 70 W for about 1 h and no visible damage is found either. The fiber diameter  $d$  is determined from the SEM image. During the AFM experiment, the portion of the glass fiber in contact with the liquid is further cleaned by ethanol prior to each measurement to ensure that the force measurements are reproducible for each fluid sample.

### C. Preparation of liquid interface

The liquid-air interface is prepared using a stainless steel well 10 mm in diameter and 5 mm in depth. The well has a sharp circular edge to pin the liquid-air interface in order to reduce unwanted surface flow. The stainless steel cell is mounted inside a closed AFM liquid cell. Prior to each measurement, the sample cell is thoroughly cleaned following the procedures as described in Ref. [22]. The entire liquid cell is sealed with a flexible rubber diaphragm to minimize the evaporation of the liquid sample. A stepper motor is used to move the entire liquid cell toward the AFM cantilever with an accuracy  $0.1 \mu\text{m}$ .

The properties of the 28 liquid samples used in the experiment are given in Table I. These liquids were chosen because their interfacial properties are stable and a wide range of interfacial tensions and contact angles are covered. The values of  $\theta_a$  and  $\theta_r$  for different liquids with a freshly plasma-cleaned glass fiber are obtained using Eq. (1).

### D. AFM operation

Measurements of the capillary force  $f$  are conducted using an AFM (MFP-3D, Asylum Research) under the contact mode. All of the cantilevers used in the experiments are calibrated individually using the thermal power spectral density method. All the AFM experiments are conducted in a lab room

with a vibration-isolation floor. In addition, the entire AFM system sits on an active vibration-isolation table, which further reduces the effect of surrounding vibrations.

For a typical value of  $f = 100 \text{ nN}$  and  $k = 2 \text{ N/m}$ , we find the vertical displacement  $\delta z$  of the cantilever itself due to its deflection under the action of  $f$  is  $\delta z \simeq 100 \text{ nN}/(2 \text{ N/m}) = 50 \text{ nm}$ . This value of  $\delta z$  is negligibly small compared to the typical traveling distance  $s$  of the hanging fiber, which is of the order of micrometers. The corresponding angular deflection for a rectangular cantilever with a beam length  $\ell = 200 \mu\text{m}$  is  $\delta\theta = \arctan[\delta z/\ell] \simeq 0.01^\circ$ . This value of  $\delta\theta$  is so small that it will not affect the vertical orientation of the hanging fiber relative to the liquid-air interface.

The hanging fiber probe can also be used to directly measure the surface tension  $\gamma$ . This is achieved by slowly pulling the glass fiber out of the liquid-air interface and finding the maximum value of the measured capillary force  $f_m$  just before the fiber detaches from the liquid interface. When the CL reaches the tip of the glass fiber, it is pinned by the sharp edge of the fiber end. As the fiber is further pulled upward, the meniscus is stretched, causing the capillary force  $f$  to increase and the contact angle  $\theta_i$  to decrease until the meniscus becomes parallel to the fiber surface (i.e.,  $\theta_i = 0$ ) [27]. At this point, the measured  $f$  reaches the maximum value,  $f_m = \pi d\gamma$  [see Eq. (1)]. The value of  $\gamma$  can be calculated using this equation when the value of  $d$  is known. With this method, we are able to obtain the correct values of  $\gamma$  for the liquids listed in Table I when compared with their literature values.

## III. EXPERIMENTAL RESULTS

Figure 2(a) shows a typical hysteresis force loop obtained at a water-air interface. An uncleaned glass fiber is used here so fluctuations of the capillary force are enlarged by the large heterogeneity spots on the glass surface. The red curve shows how the measured  $f$  changes when the glass fiber is pushed downward ( $\rightarrow$ ) at a constant speed  $U = 0.1 \mu\text{m/s}$ . Before the start of the motion, the fiber was already partially immersed in the water and the contact line was pinned on the fiber surface. When the fiber advances, the pinned interface is stretched, causing a linear increase of  $f$  with the distance traveled  $s$ , as shown by a straight line at the beginning of the red curve. When the restoring force becomes larger than the pinning force, the contact line begins a stick-slip motion, as evidenced by the horizontal fluctuations in the force curve. When the direction of motion is reversed ( $\leftarrow$ ), the same pinning-depinning is repeated, as shown by the black receding curve in Fig. 2(a). Figure 2(a) reveals some interesting generic features, which were also observed in the hysteresis loop of the frictional force for a softer AFM tip sliding over a hard solid surface [30]. It is seen that the steady-state force fluctuations have a sawtoothlike symmetry with a slow accumulation of force followed by a sharp release. This effect is observed in both advancing and receding directions, as marked by the two small boxes in Fig. 2(a). Furthermore, the local pinning-depinning events in the advancing curve occur at locations that differ from those in the receding curve.

Figure 2(b) shows a side-by-side comparison of the steady-state advancing ( $\rightarrow$ ) and receding ( $\leftarrow$ ) traces obtained on the same segment of a cleaned glass fiber in octanol. Although

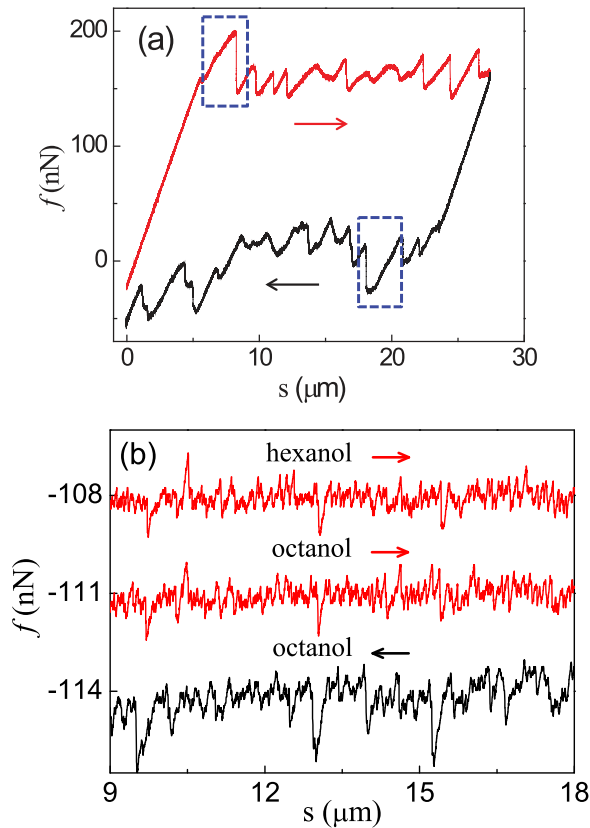


FIG. 2. (a) Variations of the measured capillary force  $f$  when an uncleaned glass fiber is pushed downward [red advancing ( $\rightarrow$ ) curve] and is pulled upward [black receding ( $\leftarrow$ ) curve] through a water-air interface. (b) Comparison of the steady-state red advancing ( $\rightarrow$ ) and black receding ( $\leftarrow$ ) traces obtained on the same segment of a cleaned glass fiber at the octanol-air and hexanol-air interfaces. For clarity, the top red curve is shifted +2 nN and the bottom black curve is shifted +3.5 nN.

the measured  $f_h$  for the octanol-air interface is much smaller than that for the water-air interface, the differences between the advancing and receding traces are clearly observable. Figure 2(b) also shows a side-by-side comparison of two steady-state advancing traces ( $\rightarrow$ ) obtained on the same segment of the fiber in hexanol (upper red curve) and in octanol (lower red curve). The two traces reveal almost identical force fluctuations, confirming that these force fluctuations are the “fingerprints” of the same surface heterogeneity. It is also found that even for a cleaned glass fiber, there are still some large intrinsic defects on the fiber surface, which give rise to a number of large spikes in the measured force curve (not shown in Fig. 2). These large force spikes are reproducible in both the advancing and receding directions and become a unique set of position markers for the glass fiber under study. In the experiment, we use these position markers to align the advancing and receding curves, as shown in Fig. 2(b).

From the measured hysteresis force loop in Fig. 2(a), we obtain two characteristic properties of the hysteresis loop. The first is the capillary force difference  $f_h$  per unit length given in Eq. (2), which is obtained from the mean value of the upper and lower sides of the hysteresis loop. Figure 3 shows how the measured  $f_h$  changes with  $\gamma \sin \theta_0$  for 27

different liquid samples. Because the equilibrium contact angle  $\theta_0$  is not known *a priori*, we estimate its value via the equation,  $\cos \theta_0 \simeq (\cos \theta_a + \cos \theta_r)/2$ . In addition to a simple hydrocarbon (decane) and a fluorocarbon (FC77), we also use a variety of organic liquids with varying head groups, including alcohol, amine, benzene, and weak acid, as shown in Table I. To have a better comparison, some of the measurements were made using the same portion of the glass fiber. In fact, the measured  $f_h$  is found to be invariant with the location of the fiber surface and is not sensitive to the fiber speed  $U$  in the range studied (0.1–10  $\mu\text{m/s}$ ). Six organic liquids including decane and FC77 are found to be of approximately zero hysteresis ( $f_h \simeq 0$ ) and their contact angle is also approximately zero. All the data points in Fig. 3 superimpose onto a single master curve, suggesting that the measured  $f_h$  for different liquids is determined by a common mechanism, which will be discussed in Sec. IV below.

The second property is the elastic restoring force shown on the left and right sides of the hysteresis loop, which is generated by stretching the pinned meniscus around the fiber. As shown in Fig. 2(a), the linear variation of  $f$  is very smooth, indicating that the CL pinning is strong and no visible slip occurs. When the fiber is pulled upward (or pushed downward) by a small distance  $dz$ , the contact angle is reduced (increased) and the resulting restoring force becomes  $F_s \simeq K_s dz$ , where  $K_s$  is the spring constant of the (deformed) meniscus. Figure 4 shows the measured  $K_s/\gamma$  as a function of  $\sin \theta_0$  for 16 organic liquid samples. Here  $\theta_0$  is determined in the same way as for Fig. 3. There are two values of  $K_s$  for each hysteresis loop; one is from the advancing trace and the other is from the receding trace. These two values of  $K_s$  are found to be approximately the same for all the liquid samples studied. The error bars in Fig. 4 show the typical differences between the two values of  $K_s$  obtained in the advancing and receding directions.

In Fig. 4, we also include four data points obtained when the glass fiber is placed in water for a while up to an hour.

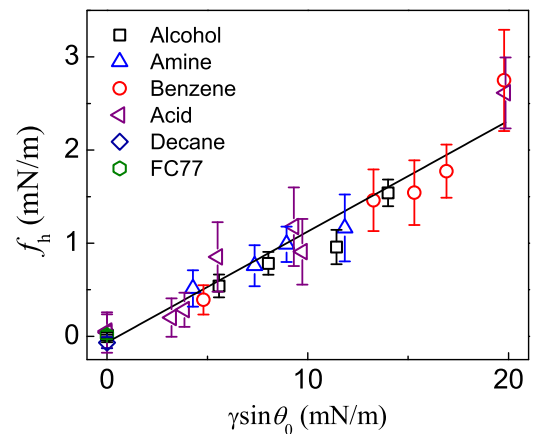


FIG. 3. Measured  $f_h$  as a function of  $\gamma \sin \theta_0$  for 27 organic liquid samples: OH- $C_nH_{2n+1}$  (alcohol, squares), NH<sub>2</sub>- $C_nH_{2n+1}$  (amine, up-triangles), benzene derivatives (benzene, circles), COOH- $C_nH_{2n+1}$  (acid, left triangles), decane (diamond), and FC77 (hexagon). The error bars show the standard deviation of the steady-state force fluctuations. The solid line is a linear fit to the data points.

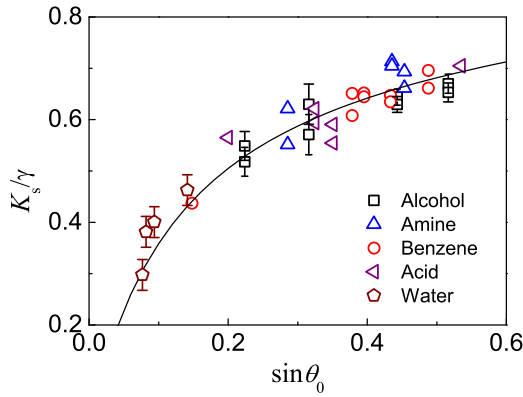


FIG. 4. Measured  $K_s/\gamma$  as a function of  $\sin\theta_0$  for 17 different liquid samples. Symbols used are the same as those in Fig. 3 (with pentagons for water in addition). The solid line is a plot of Eq. (14).

During this period of time, the capillary force hysteresis starts to grow slowly and we measure the hysteresis force loop (and hence the values of  $K_s$ ,  $\gamma$  and  $\sin\theta_0$ ) at different time lapses. It is found that the capillary force hysteresis increases from  $\sim 0$  to  $\sim 80$  nN after the glass fiber is immersed in water for 3 h. We believe that the increase of the hysteresis is due to a slow chemical reaction on the glass surface in contact with water (e.g., surface ionization), which gives rise to a slow change of the water-glass interfacial tension (and hence the contact angle  $\theta_i$ ). It is also found that the surface tension of the water-air interface decreases with time slowly, most likely due to contaminations at the water-air interface. This occurs after the glass fiber is immersed in water for more than an hour. Figure 4 reveals that all the data points superimpose onto a single master curve, which is well described by Eq. (14) (solid line) to be given below.

#### IV. FURTHER ANALYSIS AND DISCUSSIONS

##### A. Contact angle hysteresis on an ambient solid surface

Theoretical models explain CAH based on a mechanical balance between the elastic restoring force due to the deformation of the liquid interface and the pinning force produced by surface heterogeneities [4]. For a single defect, the JG model [10] predicted two typical hysteresis force loops, which are presented graphically in Fig. 5(a). When a MCL approaches a single nonwetting (repulsive) defect located at  $s_1$ , it is opposed (or pinned) by the defect so the force  $f$  acting on the substrate increases with moving distance  $s$ , having a slope equal to the effective spring constant of the deformed contact line (red curve in the left loop). This situation lasts until the elastic restoring force cannot be balanced by the pinning force anymore. On the receding (black curve in the left loop), the CL will snap off from the defect (i.e., the CL slips), causing a sudden jump in  $f$  at  $s_1$  (with a small shift less than the defect size  $w$ ). Because the magnitude of  $f$  decreases with further increase of  $s$  (moving away from the defect), there is only a very weak pinning force in the receding direction. The asymmetry between the advancing (red) and receding (black) curves was used to explain CAH [10,26]. The situation is reversed for a wetting (attractive) defect, as shown by the right loop in Fig. 5(a). For CAH on a random surface, the red curve

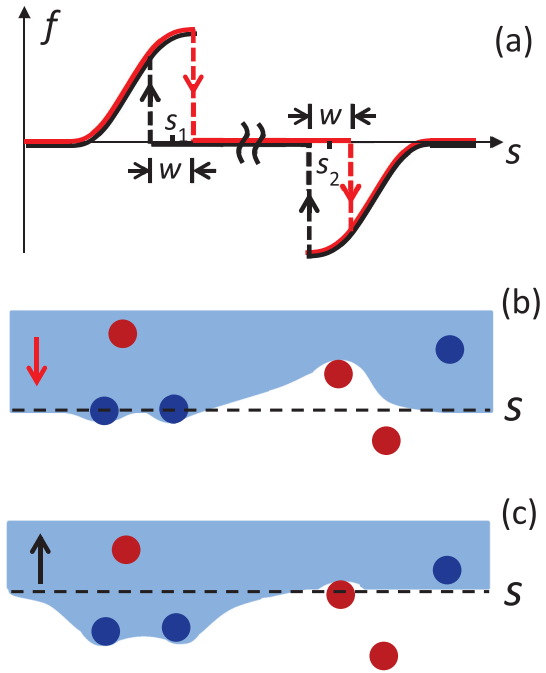


FIG. 5. (a) Construction of typical hysteresis force loops based on the Joanny–de Gennes model for a single repulsive defect of size  $\sim w$  at  $s_1$  (left loop) and a single attractive defect at  $s_2$  (right loop). Red (black) curves show the advancing (receding) traces. [(b) and (c)] Top view of a deformed contact line pinned by an array of repulsive [red (light gray) dots] and attractive [blue (dark gray) dots] defects. The shaded area indicates the area occupied by the fluid and the dashed line indicates the mean position of the moving contact line (b) in the advancing direction and (c) in the receding direction.

in the left loop corresponds to the situation when an advancing CL approaches a nonwetting region of the solid surface. When a receding CL approaches the same nonwetting region, the force is depicted by the black curve in the left loop. Similarly, the pinning of a CL by a wetting region can be qualitatively described by the right loop.

Evidently, the measured hysteresis loop in Fig. 2(a) does not have the basic symmetry as predicted by either of the loops shown in Fig. 5(a). Instead, the measured advancing curve has a symmetry similar to the red curve for a relatively nonwetting (repulsive) defect (region) and the receding curve has a symmetry similar to the black curve for a relatively wetting (attractive) defect (region). Thus the two curves are linked by two different types of defects on the surface. Based on these observations, we propose a “composite model” of CAH for an ambient solid surface, which contains two sets of coexisting and spatially intertwined defects with opposite natures. The two types of defects can be generated either by the positive and negative fluctuations of chemical heterogeneity relative to the mean or by the physical roughness of the surface with grooves and ridges. These defects give rise to a complex landscape of a relatively nonwetting (repulsive) force field (red dots) intertwined with a relatively wetting (attractive) one (blue dots), as illustrated in Fig. 5(b) [and Fig. 5(c)]. Because the red dots provide the largest pinning in the advancing direction, the advancing CL is pinned predominantly by the red dots,

which produce larger CL deformations than those made by the blue dots [see Fig. 5(b)]. Therefore, the corresponding force curve will have a symmetry similar to the red curve of the left loop in Fig. 5(a). Similarly, the CL in the receding direction will be pinned predominantly by the blue dots, as indicated in Fig. 5(c). Our model thus explains the sawtooth-like symmetry of the observed force fluctuations in the advancing and receding directions.

The above “composite model” can also be illustrated with an effective landscape experienced by the entire CL (assuming in the  $x$  direction). Figure 6 shows a one-dimensional (1D) presentation of the complex landscape (gray curve) consisting of intertwined positive (nonwetting) and negative (wetting) fluctuations of the defect force relative to a mean value  $F_0$ . Following Refs. [10,31], the mechanical balance between the elastic restoring force of the deformed liquid interface and the landscape of positive (negative) defect forces gives rise to an advancing (receding) trace as shown by the red (black) curve in Fig. 6. Here we have assumed that the CL moves along its normal direction ( $y$  direction). The solid portion of the red and black curves corresponds to the pinning of the CL moving in the advancing ( $\rightarrow$ ) and receding ( $\leftarrow$ ) directions, respectively, and the dashed portion of the two curves represents the slip of the CL to another defect. The slope of the dashed lines indicates the effective spring constant of the deformed liquid interface. Such local pinning-depinning events result in a stick-slip-like motion of the CL, as shown in Fig. 2. Because the solid traces provide the largest pinning, the CL is actually pinned by the positive (nonwetting) defects in the advancing direction and by the negative (wetting) defects in the receding direction. These two sets of coexisting and spatially intertwined defects with opposite natures therefore produce two different values of the contact angle (or capillary force) depending on the moving direction of the CL.

Although the above arguments are made for smooth but chemically heterogeneous surfaces, modeling of surface roughness is mathematically similar to that for chemical heterogeneity [3]. Therefore, the composite model is also applicable to rough surfaces, where grooves and ridges act

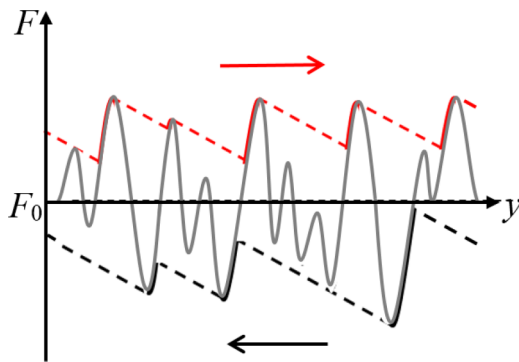


FIG. 6. A one-dimensional presentation of the complex landscape (gray curve) consisting of intertwined positive (repulsive) and negative (attractive) fluctuations of the defect force relative to a mean value  $F_0$ . The red advancing and black receding curves illustrate the pinning and depinning events as explained by the “composite model” of contact angle hysteresis (see text for more explanations).

like nonwetting and wetting defects, respectively [5]. Previous studies of CAH have considered chemically patterned surfaces composing of parallel alternating A-B stripes of equal width but with different wetting properties [32–35]. In these studies, the CL was assumed to be parallel to the stripe boundaries and thus sequentially encounters two different types of boundary defects as it moves. This is a simplified model for a 1D periodic array of defects, as the CL only encounters a single step jump of contact angle (or energy barrier) at any given time. The composite model, on the other hand, is concerned with a 2D random array of defects, and thus the CL simultaneously encounters a large number of different defects, as indicated in Fig. 5(b). In this case, because of the energetic competition between the relatively wetting and nonwetting defects, the microscopic position of the CL [ $y(x,s)$  in Eq. (8) below] becomes dependent on the moving direction of the CL.

Nonetheless, the simplified model for parallel alternating A-B stripes is a good starting point for the study of CAH. By a careful energetic analysis, the previous studies [33,35] have shown analytically that CL pinning occurs only when the advancing CL crosses the A-B boundary from a relatively wetting region with a small contact angle to a relatively nonwetting (repulsive) region with a larger contact angle. During the crossover event, the CL retains at a unique minimum energy state by adjusting the shape of the liquid interface. Similarly, the CL pinning was also found when the receding CL moves from a relatively nonwetting surface with a large contact angle to a relatively wetting (attractive) surface with a smaller contact angle. When this condition is not satisfied, the CL moves across the A-B boundary by a sudden change of its contact angle, i.e., CL slip occurs. In this case, the CL jumps from a local minimum energy state to another local minimum energy state. These analytical results reached the same conclusion as illustrated in Fig. 5(a) and thus are consistent with the above composite model as far as the 1D defect case is concerned. It would be of great interest to extend the mathematical analysis and computer simulation to 2D chemically patterned surfaces, which have more interesting features closer to the actual solid surfaces used in experiment.

## B. Surface structures of the glass fiber

As discussed in Sec. III, the hysteresis force loop shown in Fig. 2(a) was obtained on an uncleaned glass fiber, which is found to be hydrophobic with  $\theta_i \gtrsim 90^\circ$  ( $f \gtrsim 0$ ) and has a large CAH. In this case, the heterogeneity spots on the fiber surface produce large fluctuations of the capillary force both in amplitude and in lateral extent, allowing us to clearly observe the sawtooth-like symmetry of the steady-state force fluctuations in both the advancing and receding directions. While Fig. 2(a) is very useful to reveal the basic features of the hysteresis force loop, it is quite difficult to use a uncleaned glass fiber to carry out systematic studies of CAH. We therefore use the plasma cleaning procedure as described in Sec. II to prepare the glass fibers with reproducible surface features. As mentioned above, the freshly plasma-cleaned glass fiber shows no hysteresis in water with  $\theta_0 \simeq 0^\circ$ . Even for this chemically homogeneous fiber surface, we still observed considerable CAH for a variety of liquids listed in Table I, indicating that the observed CAH for the plasma-cleaned glass fiber is caused

primarily by the surface roughness, which remains the same for different liquids.

To examine the actual surface morphology, we conduct AFM measurements of surface topology of the glass fiber used in the experiment. Figure 7 shows a typical AFM topographic image of the top surface of a glass fiber lying on a flat substrate. While the fiber surface is relatively smooth, it is nevertheless superimposed with a roughness landscape consisting of intertwined ridges (white) and troughs (dark) of typical (symmetric) height  $\pm 0.4$  nm and domain size 20–50 nm. Except for Fig. 2(a), all of the experimental results reported here, including those shown in Figs. 3 and 4, are obtained using the plasma-cleaned glass fibers.

### C. Capillary force hysteresis for a contact line

As discussed in Sec. IV A, because the advancing force  $f_a$  and receding force  $f_r$  are determined by two different sets of relatively wetting and nonwetting defects on the surface, the actual magnitude of  $f_a$  and  $f_r$  will depend on the nature and density of each set of the defects separately. This conclusion thus can be used to explain the asymmetric behavior of CAH observed on surfaces with either nonwetting (repulsion) dominant or wetting (attraction) dominant defects. For example, Priest *et al.* [15] reported that the CAH of the synthetic “high-energy” defects (i.e., wetting dominant defects) in the receding direction behaves similarly to that of the “low-energy” defects (i.e., nonwetting dominant defects) in the advancing direction. From the experiments using superhydrophobic surfaces consisting of a regular array of micropillars [36–38], it was found that the relatively wetting micropillars (compared to the air) cause significant CL pinning in the receding direction and give rise to CAH.

When the distribution of the two sets of defects is symmetric, such as that shown in Fig. 7, the unbalanced capillary force,  $|f_i - f_0|$ , needed to depin the CL and move it in the advancing direction ( $i = a$ ) is equal to that in the receding direction ( $i = r$ ). This condition implies that  $f_0 = (f_a + f_r)/2$ , which is used in the experiment to define the equilibrium contact

angle  $\theta_0$  ( $\cos \theta_0 = (\cos \theta_a + \cos \theta_r)/2$ ). This definition of  $\theta_0$  has also been used in previous studies [17,18]. In this case, one has

$$\pi d f_h \equiv |f_a - f_r| \equiv |(f_a - f_0) + (f_0 - f_r)| \simeq 2|f_i - f_0|, \quad (3)$$

where  $f_0 = \pi d \gamma \cos \theta_0$  is the (unpinned) reference state. Macroscopically, one can write down the unbalanced capillary force as [39],

$$|f_i - f_0| = \pi d \gamma |\cos \theta_i - \cos \theta_0| \simeq \pi d \gamma \sin \theta_0 \sin(\delta\theta_i), \quad (4)$$

where  $f_i$  is the mean value of the measured capillary force at its steady state, as shown in Fig. 2. In the above, we have assumed that the contact angle change,  $\delta\theta_i = |\theta_i - \theta_0|$ , is small. With Eqs. (3) and (4) the capillary hysteresis force becomes

$$f_h \simeq 2\gamma \sin \theta_0 \sin(\delta\theta), \quad (5)$$

where the subscript  $i$  in  $\delta\theta$  is dropped, because  $\delta\theta = \delta\theta_a = \delta\theta_r$  when  $|f_a - f_0| = |f_r - f_0|$ .

As shown in Fig. 3, the measured  $f_h$  agrees well with the scaling law predicted in Eq. (5). It is a linear function of  $\gamma \sin \theta_0$  for small values of  $\gamma \sin \theta_0$  (solid line in Fig. 3), indicating that  $\sin(\delta\theta)$  in Eq. (5) is a constant for all the 27 liquid samples used. This finding further confirms that the measured  $f_h$  (or  $|f_i - f_0|$ ) is caused primarily by the surface roughness of the glass fiber. In this case,  $\sin(\delta\theta)$  only involves local roughness variations, which are independent of the liquid samples used [6,10,17]. The value of  $\sin(\delta\theta)$  will change with the fluid samples used if chemical heterogeneity were involved. This is because the liquid-solid interfacial tension is changed when different fluids are used. From the slope of the solid line in Fig. 3, we find  $\sin(\delta\theta) \simeq 0.06$ .

In deriving Eq. (4) we have assumed that the defect-induced contact angle variation  $\delta\theta_i$  is small so  $|\cos(\theta_0 + \delta\theta_i) - \cos \theta_0| \simeq \sin \theta_0 \sin(\delta\theta_i)$ . In other words, Eq. (4) only gives the first-order expansion of  $|\cos(\theta_0 + \delta\theta_i) - \cos \theta_0|$ . This “weak pinning” assumption is supported by our finding that  $\sin(\delta\theta) \simeq 0.06$ . It is seen from Fig. 7 that the fiber surface is quite smooth with a roughness height of  $\sim 0.4$  nm over an area of size 20–50 nm. In addition, we find from Table I that the measured contact angle hysteresis,  $\theta_a - \theta_r$ , for most fluid samples is in the small range  $1^\circ$ – $7^\circ$ . With the defect size  $\lambda \simeq 20$  nm and hysteresis force  $f_h \simeq 1$  mN/m (see Fig. 3), we estimate the energy involved for the CL pinning as [40]  $E_b \simeq (f_h/2)(\lambda/2)^2 \simeq 12k_B T$ , where  $k_B T$  is the thermal energy. These findings suggest that each individual defect is probably not big enough to pin the CL but collectively the roughness defects are able to pin the CL [17,19,31].

It is also seen from Fig. 3 that although most of the data points are well described by a linear function (solid line), the two data points with the largest value of  $\gamma \sin \theta_0$  show considerable deviations from the solid line. The two data points are obtained for benzyl alcohol (red circle) and formic acid (purple triangle), which also show large contact angle hysteresis with  $\theta_a - \theta_r$  in the range  $8.1^\circ$ – $13^\circ$  (see Table I). For such large contact angle hysteresis, the first-order expansion in Eq. (4) is not adequate and higher-order terms may be needed.

To connect the macroscopic parameter  $\sin(\delta\theta)$  with the microscopic details of the surface roughness, we consider a topological defect with a maximal local slope  $\varphi$  relative to the

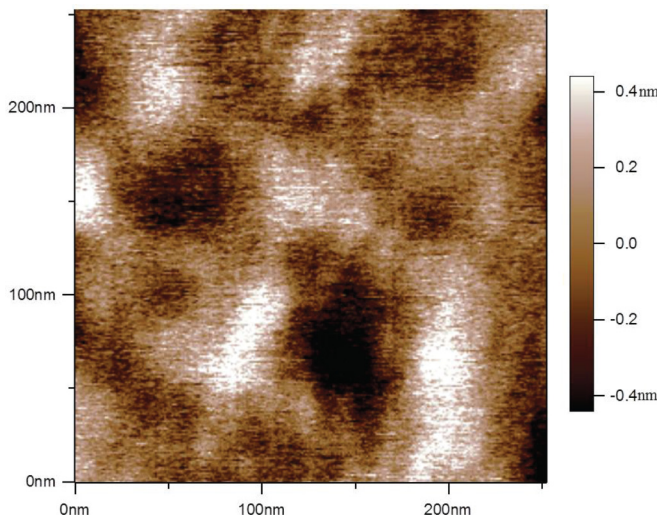


FIG. 7. AFM topographic image of the top surface of a glass fiber lying on a flat substrate. Typical height contrast is  $\pm 0.4$  nm.

substrate. The corresponding change of the capillary force  $\delta f_d$  can be written as [6,17,19],

$$\delta f_d = \gamma [\cos(\theta_0 - \varphi) - \cos \theta_0] dx \simeq \gamma \sin \theta_0 \sin \varphi dx, \quad (6)$$

where  $\theta_0$  is the contact angle relative to the substrate and  $dx$  is the size of the defect. Assuming the CL interacts with a number of defects simultaneously with its average direction along the  $x$  direction, we obtain the net capillary force per unit length acting on the CL,

$$\begin{aligned} f_d(s) &\simeq \frac{1}{\pi d} \int dx \gamma \sin \theta_0 \sin[\varphi(x, y(x, s))] \\ &= \gamma \sin \theta_0 \langle \sin[\varphi(x, s)] \rangle_x, \end{aligned} \quad (7)$$

where

$$\langle \sin[\varphi(x, s)] \rangle_x = \frac{1}{\pi d} \int_0^{\pi d} dx \sin[\varphi(x, y(x, s))], \quad (8)$$

and  $y(x, s)$  is the (microscopic) position of the CL at  $x$  for a given fiber height  $s$ . In the above, we have assumed that the local contact angle variation  $\varphi(x, y)$  is a smooth-varying function (no sharp kinks on the surface), so it is well defined at any spatial point  $(x, y)$ . Because of CAH,  $y(x, s)$  is not a single-valued function. The position of the CL depends on the direction of its motion. As discussed above on the composite model, the (microscopic) location of an advancing CL tends to be trapped by nonwetting defects, whereas, for a retreating CL,  $y(x, s)$  picks up wetting defects.

Equation (7) has several important implications. First,  $\langle \sin[\varphi(x, s)] \rangle_x$  contains all the information about the spacial averaging of the defects along the CL ( $x$  direction) and dynamic variations of a MCL as it sweeps over the defect landscape along its travel direction  $s$ . Herein we focus our attention on the mean value of  $f_d(s)$ ,

$$\begin{aligned} \langle f_d(s) \rangle_s &\simeq \frac{\gamma \sin \theta_0}{\ell_y} \int_0^{\ell_y} ds \langle \sin[\varphi(x, s)] \rangle_x \\ &= \gamma \sin \theta_0 \langle \sin[\varphi(x, s)] \rangle_{x,s}, \end{aligned} \quad (9)$$

where  $\ell_y$  is the traveling distance of the CL over which  $f_d(s)$  is averaged. Physically,  $\langle f_d(s) \rangle_s$  is determined by the static ‘‘rupture force’’ needed to overcome the energy barriers imposed by the defects and depin the CL [31,40,41]. By comparing Eq. (9) with Eq. (5), one immediately finds  $f_h \simeq 2\langle f_d(s) \rangle_s$  and

$$\sin(\delta\theta) = \langle \sin[\varphi(x, s)] \rangle_{x,s}. \quad (10)$$

Although Eq. (9) is derived by assuming the defects result from surface roughness, a similar expression can also be obtained for the CAH induced by chemical heterogeneity [2,4,6].

Second, for a symmetric distribution of surface defects such as those shown in Fig. 7, the average value  $\langle \sin[\varphi(x, s)] \rangle_{x,s}$  should be zero if the CL sensed fluctuations of  $\varphi$  in both directions. The fact that the measured  $\langle \sin[\varphi(x, s)] \rangle_{x,s}$  is nonzero, as shown in Fig. 3, provides a further support to the composite model, which states that the advancing (and receding) CL only senses  $\varphi(x, y)$  in one direction.

Finally, for weak collective pinning, Robbins and Joanny [4,31] predicted that

$$f_h \simeq \langle \delta S^2 \rangle / \gamma \sin^2 \theta_0, \quad (11)$$

where  $\langle \delta S^2 \rangle \simeq (\gamma \sin \theta_0)^2 \langle \sin^2[\varphi(x, s)] \rangle_{x,s}$  is the standard deviation of spatial variations of surface roughness. For this expression to agree with the experimental results shown in Fig. 3,  $\langle \sin^2[\varphi(x, s)] \rangle_{x,s}$  needs to be proportional to  $\sin \theta_0$ . At the moment, we cannot find any argument to support such a relation.

Like many interfacial phenomena, measurement of the capillary force involves an average over the entire CL, and thus microscopic details about the defect landscape are needed in order to fully explain the macroscopic measurement. In Fig. 3, we focus on the overall scaling dependence of the measured  $f_h$  on the experimentally controllable (macroscopic) parameters, such as the surface tension  $\gamma$  and contact angle  $\theta_0$ , recognizing that the absolute value of  $f_h$  and its fluctuations may depend on details about the defect landscape as well as the dynamics of the CL. As indicated in Fig. 2,  $\langle \sin[\varphi(x, s)] \rangle_x$  contains fluctuations as the CL moves along its normal direction  $s$ , which may involve such interesting dynamics as possible avalanche-like dynamics [42,43]. Further theoretical modeling of  $\langle \sin[\varphi(x, s)] \rangle_x$  is needed in order to understand how it depends on the CL dynamics. It is also of great interest to know how the scaling of the measured  $f_h$  changes with increasing roughness. While these topics are important in their own right, they are beyond the scope of the present paper.

#### D. Spring constant of a liquid interface pinned on a vertical glass fiber

As shown in Fig. 2(a), the linear variation of the measured  $f$  with the traveling distance  $s$  is caused by stretching the pinned liquid interface. The meniscus of the liquid interface around a stationary micron-sized fiber has zero mean curvature when the gravity effect is ignored, and it takes the form [44]

$$r(h) = b \cosh \left[ \frac{h}{b} - \ln \left( \frac{2\ell_c}{b} \right) \right], \quad (12)$$

where  $h$  is the meniscus height,  $r$  is its radial location, and  $b = (d/2) \cos \theta_0$ . The capillary length  $\ell_c = \sqrt{\gamma/\rho g}$  is used to set the cut-off length of the horizontal extent of the meniscus. The capillary rise  $h_0 \equiv h(r = d/2)$  can be obtained by inverting the above expression,

$$h_0 = \frac{d \cos \theta_0}{2} \ln \left[ \frac{2\ell_c}{d(1 + \sin \theta_0)/2} \right]. \quad (13)$$

When a CL is firmly pinned on the fiber surface and the fiber is pulled upward by a small distance  $dz$ , as shown in Fig. 8(a), the contact angle is changed to  $\theta_0 + \delta\theta$  and the resulting restoring force is  $F_s = \gamma [\cos(\theta_0 + \delta\theta) - \cos \theta_0] \simeq -K_s dz$ , where  $K_s$  is the spring constant of the (deformed) meniscus. By a linear expansion of Eq. (13), we obtain the relation between  $\delta\theta$  and  $dz$  and find

$$\frac{K_s}{\gamma} \simeq \frac{2\pi \sin \theta_0}{1 - \sin \theta_0 \{1 + \ln[(b/2\ell_c)(1 + \sin \theta_0)]\}}. \quad (14)$$

Equation (14) states that the ratio  $K_s/\gamma$  depends mainly on  $\sin \theta_0$  and is not very sensitive to  $d/2\ell_c$ , as the value of  $\ln(d/2\ell_c)$  does not change much for the fluid samples in Table I. As shown in Fig. 4, the data are well described by Eq. (14) (solid line) without any adjustable parameter, and

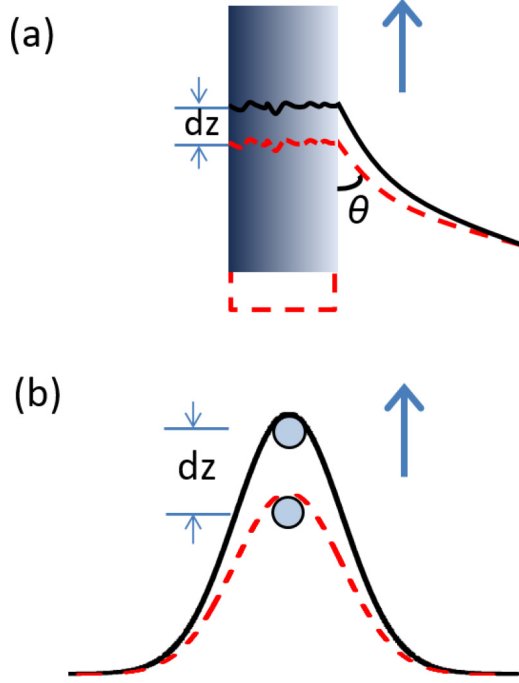


FIG. 8. (a) Deformation of a liquid-air interface, which is pinned on a glass fiber moving upward by a distance  $dz$ . (b) Deformation of a contact line pinned by a single defect (gray dot) moving upward by a distance  $dz$ .

thus an excellent agreement is obtained between the theory and experiment.

Like many interfacial rheology measurements, the geometry of the liquid interface (or the shape of the CL) determines the coefficient between  $K_s$  and  $\gamma$ . As indicated in Fig. 8(a), the CL has a circular shape, which has little deformation under an external force as it is firmly pinned by a large number of defects. The pinning defects on the CL may also introduce additional, azimuthal-angle-dependent perturbations (“ripples”) to the otherwise smooth meniscus, as depicted in Fig. 8(a). However, the length scale involved for the ripples is of the order of the defect size  $\lambda \simeq 20$  nm (see Fig. 7), whereas the length scale involved for the capillary rise goes as the fiber diameter  $d \simeq 2$   $\mu\text{m}$ . Because of the small length ratio  $\lambda/d \simeq 0.01$ , the effect of the ripples to the spring constant  $K_s$  is expected to be very small. This argument is further justified by the good agreement between the theoretical prediction in Eq. (14) (without the ripple effect) and the experimental data shown in Fig. 4.

The situation changes considerably for the single defect case, in which moving the defect by a distance  $dz$  will introduce a shape change of the CL, as indicated in Fig. 8(b). Consequently, the spring constant  $K_1$  of the liquid interface pinned by a single defect has a form that differs from Eq. (14) [10,19],

$$\frac{K_1}{\gamma} = \frac{\pi \sin^2 \theta_0}{\ln\left(\frac{L}{a}\right)}, \quad (15)$$

where  $a$  is the defect size and  $L$  is a cutoff length of the system. We also notice the difference between Eq. (14) and the elastic constant of a meniscus calculated by Jai *et al.* [45].

The calculation in Ref. [45] began with an approximation that the ratio of the capillary length  $l_c$  to the capillary rise  $h_0$  is simply the tangent of the contact angle  $\theta_0$ , i.e.,  $\tan(\theta_0 \pm \delta\theta) = l_c/(h_0 \mp dz)$ . This is a very rough estimate for the meniscus shape and it clearly differs from Eq. (13). Our prediction in Eq. (14) is derived from the exact solution of the meniscus around a stationary micron-sized fiber and thus is more accurate than that given in Ref. [45]. Again, the good agreement between Eq. (14) and the experimental results shown in Fig. 4 further supports this statement.

## V. CONCLUSION

We have carried out a systematic experimental study of CAH by direct measurement of the capillary force  $f(t)$  in Eq. (1) acting on a MCL, which is formed on the surface of a long glass fiber intersecting a liquid-air interface. The glass fiber of diameter  $d$  in the range 1–2  $\mu\text{m}$  and length 100–200  $\mu\text{m}$  is glued onto the front end of a rectangular cantilever used for AFM. By moving the fiber up and down through the liquid interface, one can accurately measure the receding force  $f_r$  (and hence the receding angle  $\theta_r$ ) and the advancing force  $f_a$  (and the corresponding advancing angle  $\theta_a$ ), respectively. CAH is then characterized by the capillary force difference per unit length,  $f_h = (f_r - f_a)/\pi d$ , given in Eq. (2). As a sensitive force apparatus, the AFM can measure the capillary force down to 10 pN with an accuracy of 0.2% and at a high sampling rate up to 1 MHz. Such a real-time measurement allows one to directly study the pinning-depinning dynamics of a MCL.

By accurately measuring the capillary force hysteresis loop of 28 different liquids with varying surface tensions and contact angles, we find a universal behavior of the elastic restoring force of the pinned liquid interface and the unbalanced capillary force in the advancing and receding directions. Based on the experimental findings, we propose a “composite model” of CAH for ambient solid surfaces with two sets of coexisting and spatially intertwined defects of opposite natures. The two types of defects can be generated either by the positive and negative fluctuations of chemical heterogeneity relative to the mean or by the physical roughness of the surface with grooves and ridges. The model presented in Fig. 5 (and also in Fig. 6) explains the basic features of the measured hysteresis force loop in Fig. 2. It is shown that the contact line is pinned primarily by the relatively nonwetting (repulsive) defects in the advancing direction and by the relatively wetting (attractive) defects in the receding direction.

From the experimental results shown in Fig. 3, we find that the measured  $f_h$  scales with  $\gamma \sin \theta_0$  with a constant slope  $\sin \delta\theta$ . This result is in good agreement with the prediction in Eq. (5). An equation is derived to connect the macroscopic parameter  $\sin(\delta\theta)$  with the microscopic details of the surface roughness. The experiment clearly demonstrates that CAH that was commonly reported in previous studies [1–4] is in fact a manifestation of capillary force hysteresis. To overcome the pinning potential imposed by the defects, different forces  $|f_i - f_0|$  are needed in order to depin the CL and keep it moving in the advancing ( $i = a$ ) and receding ( $i = r$ ) directions.

By a linear expansion of the capillary rise of the liquid meniscus around a stationary micron-sized fiber, we obtain Eq. (14), which states that the spring constant  $K_s$  associated with the stretched meniscus is proportional to the liquid-air interfacial tension  $\gamma$  and the proportionality constant depends mainly on  $\sin\theta_0$ . As shown in Fig. 4, the data are well described by Eq. (14) without any adjustable parameter, and thus an excellent agreement is obtained between the theory and experiment. Having an experimentally verified exact solution of  $K_s$  for a given geometry is very important, as it will establish a quantitative method by which many other soft interfaces

involving polymers, surfactants, and biomolecules (such as proteins and lipids) may be characterized dynamically.

#### ACKNOWLEDGMENTS

We have benefited from useful discussions with Q. He, E. Charlaix, T.-Z. Qian, X.-P. Wang, P. Sheng, J.-F. Joanny, and D. Beck. H.Y.C. acknowledges support by MOST Taiwan under Grant No. 102-2112-M-008-008-MY3. P.T. acknowledges support by the Hong Kong Research Grants Council under Grant No. HKUST605013.

- 
- [1] P.-G. de Gennes, *Rev. Mod. Phys.* **57**, 827 (1985).  
 [2] L. Leger and J.-F. Joanny, *Rep. Prog. Phys.* **55**, 431 (1992).  
 [3] E. L. Decker and S. Garoff, *J. Adhesion* **63**, 159 (1997).  
 [4] D. Bonn, J. Eggers, J. Indekeu, J. Meunier, and E. Rolley, *Rev. Mod. Phys.* **81**, 739 (2009).  
 [5] D. Quéré, *Annu. Rev. Mater. Res.* **38**, 71 (2008).  
 [6] M. Ramiasa, J. Ralston, R. Fetzer, and R. Sedev, *Adv. Colloid Interface Sci.* **206**, 275 (2014).  
 [7] E. R. Jerison, Y. Xu, L. A. Wilen, and E. R. Dufresne, *Phys. Rev. Lett.* **106**, 186103 (2011).  
 [8] A. Marchand, S. Das, J. H. Snoeijer, and B. Andreotti, *Phys. Rev. Lett.* **109**, 236101 (2012).  
 [9] R. W. Style, R. Boltyskiy, Y. Che, J. S. Wettlaufer, L. A. Wilen, and E. R. Dufresne, *Phys. Rev. Lett.* **110**, 066103 (2013).  
 [10] J.-F. Joanny and P.-G. de Gennes, *J. Chem. Phys.* **81**, 552 (1984).  
 [11] J. M. Di Meglio, *Europhys. Lett.* **17**, 607 (1992).  
 [12] G. D. Nadkarni and S. Garoff, *Europhys. Lett.* **20**, 523 (1992).  
 [13] A. Paterson, M. Fermigier, P. Jenffer, and L. Limat, *Phys. Rev. E* **51**, 1291 (1995).  
 [14] S. Moulinet, A. Rosso, W. Krauth, and E. Rolley, *Phys. Rev. E* **69**, 035103(R) (2004).  
 [15] C. Priest, R. Sedev, and J. Ralston, *Phys. Rev. Lett.* **99**, 026103 (2007).  
 [16] M. Reyssat and D. Quéré, *J. Phys. Chem. B* **113**, 3906 (2009).  
 [17] S. M. M. Ramos, E. Charlaix, A. Benyagoub, and M. Toulemonde, *Phys. Rev. E* **67**, 031604 (2003).  
 [18] S. Ramos and A. Tanguy, *Eur. Phys. J. E* **19**, 433 (2006).  
 [19] M. Delmas, M. Monthieux, and T. Ondarucu, *Phys. Rev. Lett.* **106**, 136102 (2011).  
 [20] J. A. Marsh, S. Garoff, and E. B. Dussan V., *Phys. Rev. Lett.* **70**, 2778 (1993).  
 [21] Q. Chen, E. Raméand S. Garoff, *J. Fluid Mech.* **337**, 49 (1997).  
 [22] X.-M. Xiong, S. Guo, Z.-L. Xu, P. Sheng, and P. Tong, *Phys. Rev. E* **80**, 061604 (2009).  
 [23] S. Guo, X.-M. Xiong, Z.-L. Xu, P. Sheng, and P. Tong, *Chin. Phys. B* **23**, 116802 (2014).  
 [24] S. Guo, M. Gao, X.-M. Xiong, Y. J. Wang, X.-P. Wang, P. Sheng, and P. Tong, *Phys. Rev. Lett.* **111**, 026101 (2013).  
 [25] S. Guo, C. H. Lee, P. Sheng, and P. Tong, *Phys. Rev. E* **91**, 012404 (2015).  
 [26] J.-M. Di Meglio and D. Quéré, *Europhys. Lett.* **11**, 163 (1990).  
 [27] M. M. Yazdanpanah, M. Hosseini, S. Pabba, S. M. Berry, V. V. Dobrokhotov, A. Safir, R. S. Keynton, and R. W. Cohn, *Langmuir* **24**, 13753 (2008).  
 [28] "Physical constants of organic compounds," in *CRC Handbook of Chemistry and Physics*, edited by D. R. Lide (CRC Press, Boca Raton, FL, 2005).  
 [29] M. E. Bai, K. G. Neerajakshi, K. S. V. K. Rao, G. N. Swamy, and M. C. S. Subha, *J. Indian Chem. Soc.* **82**, 25 (2005).  
 [30] R. Wiesendanger, *Scanning Probe Microscopy and Spectroscopy* (Cambridge University Press, Cambridge, UK, 1994), p. 235.  
 [31] M. O. Robbins and J. F. Joanny, *Europhys. Lett.* **3**, 729 (1987).  
 [32] R. E. Johnson and R. H. Dettre, *J. Phys. Chem.* **68**, 1744 (1964).  
 [33] M. Iwamatsu, *J. Colloid Interface Sci.* **297**, 772 (2006).  
 [34] X.-P. Wang, T.-Z. Qian, and P. Sheng, *J. Fluid Mech.* **605**, 99 (2008).  
 [35] X.-M. Xu and X.-P. Wang, *SIAM J. Appl. Math.* **71**, 1753 (2011).  
 [36] D. Oner and T. J. McCarthy, *Langmuir* **16**, 7777 (2000).  
 [37] L.-C. Gao and T. J. McCarthy, *Langmuir* **22**, 6234 (2006).  
 [38] W. Xu and C.-H. Choi, *Phys. Rev. Lett.* **109**, 024504 (2012).  
 [39] J. Snoeijer and B. Andreotti, *Annu. Rev. Fluid Mech.* **45**, 269 (2013).  
 [40] E. Rolley and C. Guthmann, *Phys. Rev. Lett.* **98**, 166105 (2007).  
 [41] T. D. Blake and J. M. Haynes, *J. Colloid Interface Sci.* **30**, 421 (1969).  
 [42] L.-H. Tang, in *Encyclopedia of Complexity and Systems Science*, edited by R. A. Meyers (Springer, New York, 2009).  
 [43] P. Le Doussal, K. J. Wiese, *Phys. Rev. E* **82**, 011108 (2010).  
 [44] P.-G. de Gennes, F. Brochard-Wyart, and D. Quéré, *Capillarity and Wetting Phenomena* (Springer, New York, USA, 2004), p. 47.  
 [45] C. Jai, J. P. Aime, and R. Boisgard, *Europhys. Lett.* **81**, 34003 (2008).